Check for updates

ADVANCED MATERIALS
www.advmat.de

Flexible All-Inorganic Thermoelectric Yarns

Hanhwi Jang, Junseong Ahn, Yongrok Jeong, Ji-Hwan Ha, Jun-Ho Jeong, Min-Wook Oh,* Inkyu Park,* and Yeon Sik Jung**

Achieving both formability and functionality in thermoelectric materials remains a significant challenge due to their inherent brittleness. Previous approaches, such as polymer infiltration, often compromise thermoelectric efficiency, underscoring the need for flexible, all-inorganic alternatives. This study demonstrates that the extreme brittleness of thermoelectric bismuth telluride (Bi_2Te_3) bulk compounds can be overcome by harnessing the nanoscale flexibility of Bi_2Te_3 nanoribbons and twisting them into a yarn structure. The resulting Bi_2Te_3 yarn, with a Seebeck coefficient of $-126.6\ \mu V\ K^{-1}$, exhibits remarkable deformability, enduring extreme bending curvatures (down to 0.5 mm^{-1}) and tensile strains of ≈5% through over 1000 cycles without significant resistance change. This breakthrough allows the yarn to be seamlessly integrated into various applications—wound around metallic pipes, embedded within life jackets, or woven into garments—demonstrating unprecedented adaptability and durability. Moreover, a simple 4-pair thermoelectric generator comprising Bi_2Te_3 yarns and metallic wires generates a maximum output voltage of 67.4 mV, substantiating the effectiveness of thermoelectric yarns in waste heat harvesting. These advances not only challenge the traditional limitations posed by the brittleness of thermoelectric materials but also open new avenues for their application in wearable and structural electronics.

1. Introduction

Flexibility is the ability of a material to exhibit excellent shape conformity without mechanical failure or rupture under tensile, compressive, or bending conditions.[1] Metals and polymers are typical materials that can be utilized flexibly, making them suitable for applications in flexible electronics, sensors, and batteries.[2] In contrast, ceramics, due to their extremely brittle nature, are limited in applications that require frequent plastic deformation or mechanical stress (**Figure 1a**).[3] Numerous efforts have been made to improve the poor mechanical properties of ceramics. For example, polymeric binders can be composited with functional ceramic particles to leverage the superior mechanical properties of polymers and the high functionality of ceramics (Figure 1b).[4] However, this approach inevitably degrades material properties because the polymeric binder typically serves only as a mechanical support and lacks functionality, especially when high electrical conductivity is required.[5] Moreover, polymers are vulnerable in extremely hot or cold environments, making it difficult to use the hybrid in such conditions.[6]

More specifically, thermoelectric (TE) materials, which are inherently brittle, ironically require excellent shape conformity for efficient heat exchange across different surfaces.[7] Conventional TE materials are typically diced into cuboidal shapes and assembled on a planar, rigid, and brittle substrate (e.g., Al_2O_3 or Si_3N_4), which is often unsuitable for absorbing heat from non-planar, curved, and uneven surfaces (e.g., metallic pipes or human skin).[8] Therefore, several strategies have been demonstrated to develop flexible thermoelectric materials and devices.[9] For example, the infiltration of elastomeric polymers, such as polydimethylsiloxane (PDMS), provided moderate flexibility to conventional rectangular TE materials

H. Jang, Y. S. Jung
Department of Materials Science and Engineering
Korea Advanced Institute of Science and Technology (KAIST)
Daejeon 34141, Republic of Korea
E-mail: ysjung@kaist.ac.kr

J. Ahn
Department of Control and Instrumentation Engineering
Korea University
Sejong 30019, Republic of Korea

Y. Jeong
Radioisotope Research Division
Korea Atomic Energy Research Institute (KAERI)
Daejeon 34057, Republic of Korea

The ORCID identification number(s) for the author(s) of this article can be found under https://doi.org/10.1002/adma.202408320

DOI: 10.1002/adma.202408320

J.-H. Ha, I. Park
Department of Mechanical Engineering
Korea Advanced Institute of Science and Technology (KAIST)
Daejeon 34141, Republic of Korea
E-mail: inkyu@kaist.ac.kr

J.-H. Jeong
Center for Nano Lithography & Manufacturing
Korea Institute of Machinery and Materials (KIMM)
Daejeon 34103, Republic of Korea
E-mail: jhjeong@kimm.re.kr

M.-W. Oh
Department of Materials Science and Engineering
Hanbat National University
Daejeon 34158, Republic of Korea
E-mail: mwoh@hanbat.ac.kr

 © 2024 Wiley-VCH GmbH

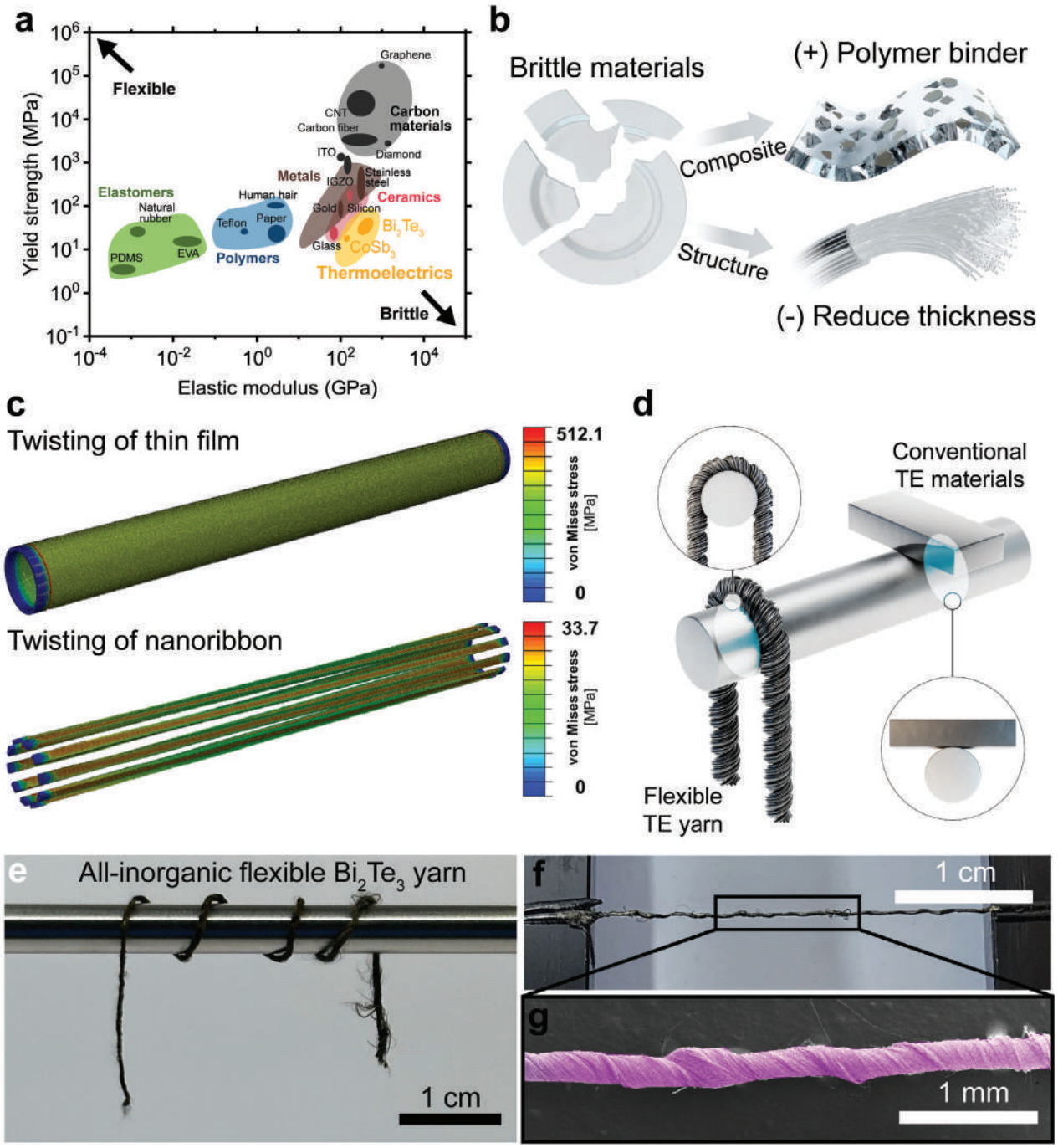


Figure 1. Roadmap for imparting flexibility to brittle materials. a) Flexibility of different materials.[14] Ceramics and TEs are representative brittle materials. b) Two representative methods to overcome poor mechanical properties of brittle materials. c) Comparison between nanofilm and nanoribbon using computational methods. In the case of twisting, the nanofilm exhibits extremely high residual stress compared to the nanoribbon. d) Twisting of nanoribbon yarn for the preparation of shape-conformable TE yarn. e) Digital photograph of Bi_2Te_3 yarn rolled along a metal tube. f–g) Digital photograph (f) and SEM image g) of as-fabricated TE yarn.

but inevitably resulted in poor TE performance due to parasitic heat loss.[4a,10] Although 3D printing of inorganic TE materials has successfully produced curved TE devices, their deformability tends to be compromised after the printing and sintering steps, making them vulnerable to frequent mechanical movements and vibration.[11] Fully inorganic yet flexible bulk semiconductor materials (e.g., Ag_2S[12] and single crystalline metal chalcogenides[13]) have been shown to address the aforementioned issues. However, the flexibility of these materials is due to specific slip mechanisms, which restrict the compositional and structural tunability, thereby limiting their potential for broader applications. Therefore, it is essential to impart flexibility to TE

© 2024 Wiley-VCH GmbH

15214095, 2024, 47, Downloaded from https://onlinelibrary.wiley.com/doi/10.1002/adma.202408320 by Korea University Medical Library, Wiley Online Library on [27/11/2024]. See the Terms and Conditions (https://onlinelibrary.wiley.com/terms-and-conditions) on Wiley Online Library for rules of use; OA articles are governed by the applicable Creative Commons License

materials to overcome the trade-off relationship between shape conformability and TE properties.

Alternatively, structural flexibility in materials can be achieved by reducing their thickness, as described by the following equation:

$$\varepsilon = h/2r_b \quad (1)$$

where ε, h, and r_b represent the maximum bending strain, the thickness of the material, and the bending radius of curvature, respectively.[14] From this equation, it is evident that as the thickness of a material decreases, the maximum bending strain also decreases when subjected to the same bending radius of curvature. Because the maximum elongation at fracture is intrinsically determined by the yield strength and Young's modulus, reducing the thickness can be a simple yet highly effective way to reduce the maximum strain resulting from the bending of material and enhance the material's ability to bend without fracturing. Accordingly, despite the high inherent brittleness of the bulk material, dramatically reducing the thickness to hundreds of nanometers of the individual nanoribbons can allow for significant softness in these structures by decreasing the degree of flexural rigidity. Utilizing this concept, several flexible thin film thermoelectric materials such as CuI,[15] $Ca_3Co_4O_9$,[16] and Fe_3CoSb_{12}[17] have been developed.

However, the limited flexibility provided by thinning is inadequate for the extremely brittle TE materials, conforming to surfaces with arbitrary geometries. For instance, the nanofilm can only conform to surfaces that maintain zero Gaussian curvature, such as planes or cylinders, and cannot be bent or twisted to adhere to surfaces with complex or irregular shapes (see Figure 1c and "Methods" for details on calculation). Additionally, TE materials with nanoscale thickness are extremely difficult to manipulate independently and can only generate a limited amount of energy, significantly limiting the performance of nanoscale TE generators as energy harvesters. Therefore, additional strategies need to be explored to assemble nanoscale materials into macroscopic clusters capable of efficiently converting sufficient heat into electricity while remaining manageable. The twisted structure of the nanoribbon yarn could be the breakthrough for both challenges. Since the nanoribbon is flexible not only along its thickness but also along the width direction, nanoribbons can conform to arbitrary surfaces, which can be directly inherited by the twisted cluster of nanoribbons. Simultaneously, twisting enables mutual support among the nanostructures and facilitates facile handling, similar to that of macrostructures (Note S1, Supporting Information).

Here, we demonstrate the realization of structurally flexible all-inorganic TE yarn by transferring nanoscale flexibility to macroscopic clusters of nanoribbons. This advancement addresses both the poor thermal contact of conventional inorganic TE materials and the limited thermal stability of polymer-infiltrated TE materials (Figure 1d). Moving beyond conventional planar TE devices, we envision the utilization of TE materials on round, rough, and soft surfaces by employing the "all-inorganic yarn" as a novel form factor for TE applications (Figure 1e). To realize the full potential of all-inorganic semiconducting TE yarns with versatile compositional tunability, we fabricate a suspended nanoribbon array by the sequential deposition of the target material onto a nanoline mold and subsequent selective removal of the mold. Controlled twisting of this array and thermal treatment produces various yarn structures, creating highly aligned, high-quality nanoribbon yarn composed of TE materials with diverse elements (such as Bi, Te, Sb, Se) in a scalable manner (Figure 1f–g). Furthermore, as a proof-of-concept application, we demonstrate the integration of the TE yarn into diverse clothing items (e.g., life jackets or sweaters), paving the way for self-powered devices in wearable electronics applications.

2. Results and Discussion

2.1. Fabrication of the All-Inorganic TE Yarn

Structurally flexible all-inorganic TE yarns were successfully fabricated using nanoimprint lithography (NIL) and precise delamination engineering, as depicted in **Figure 2a**. This methodology involves several sequential steps: First, a poly(urethane acrylate) (PUA) mold, featuring a nanoline pattern with a linewidth of 800 nm, was fabricated via NIL, as illustrated in Figure 2b. Subsequently, TE materials were deposited via electron-beam deposition in an interlayered manner, adhering to predetermined compositions and stoichiometric ratios (Steps a.1-a.3). For instance, to fabricate Bi_2Te_3 yarn, a representative high-performance TE material near room temperature,[18] alternating layers of Bi (20 nm) and Te (30 nm) were repeatedly deposited until a total of 12 layers (Bi-Te-Bi-Te-Bi-Te-Bi-Te-Bi-Te-Bi-Te) were obtained. Although assuming a proportional atomic ratio to material thickness simplifies the calculations, further refinements considering parameters such as material density and film porosity can improve the accuracy of obtaining the intended stoichiometry. After material deposition, the nanoribbon array was gently delaminated from the mold without fracture, accomplished by minimizing the adhesion forces between the mold and the deposited interlayered Bi/Te (Step a.4). This was achieved by selective and gradual etching of the nanopatterned PUA mold using O_2 and CF_4 plasma treatment, substantially reducing the adhesion forces and facilitating the easy delamination of the interlayered nanoribbon array, as shown in Figure 2c.

After delamination, the interlayered Bi/Te nanoribbon array was gently twisted into a 1D yarn using a customized yarning machine, imparting high flexibility and stretchability suitable for integration into shape-deformable and wearable devices (Step a.5). Lastly, thermal annealing at 573 K for 24 h was employed to transform the materials into a TE compound (Steps a.6-a.7). For instance, Bi_2Te_3 could be alloyed via thermal treatment of the Bi/Te interlayered nanoribbon. The ultra-thin layer thickness facilitates uniform atomic mixture by diffusion, resulting in the formation of Bi_2Te_3 compound, as depicted in Figure 2d. Notably, a variety of inorganic materials can be fabricated by changing the composition or stoichiometric ratios of the constituent elements. To demonstrate the versatility of the fabrication process, various TE materials including Bi_2Te_3, $Bi_{0.7}Sb_{0.3}$, $Bi_{1.5}Sb_{0.5}Te_3$, and $Bi_2Te_{2.7}Se_{0.3}$ were prepared with precisely controlled compositions. Scanning transmission electron microscopy (STEM) was performed to confirm nanoscale precision in thickness (before annealing) and compositional homogeneity (after annealing). We used high-angle annular dark-field (HAADF) detectors

© 2024 Wiley-VCH GmbH

15214095, 2024, 47, Downloaded from https://onlinelibrary.wiley.com/doi/10.1002/adma.202408320 by Korea University Medical Library, Wiley Online Library on [27/11/2024]. See the Terms and Conditions (https://onlinelibrary.wiley.com/terms-and-conditions) on Wiley Online Library for rules of use; OA articles are governed by the applicable Creative Commons License

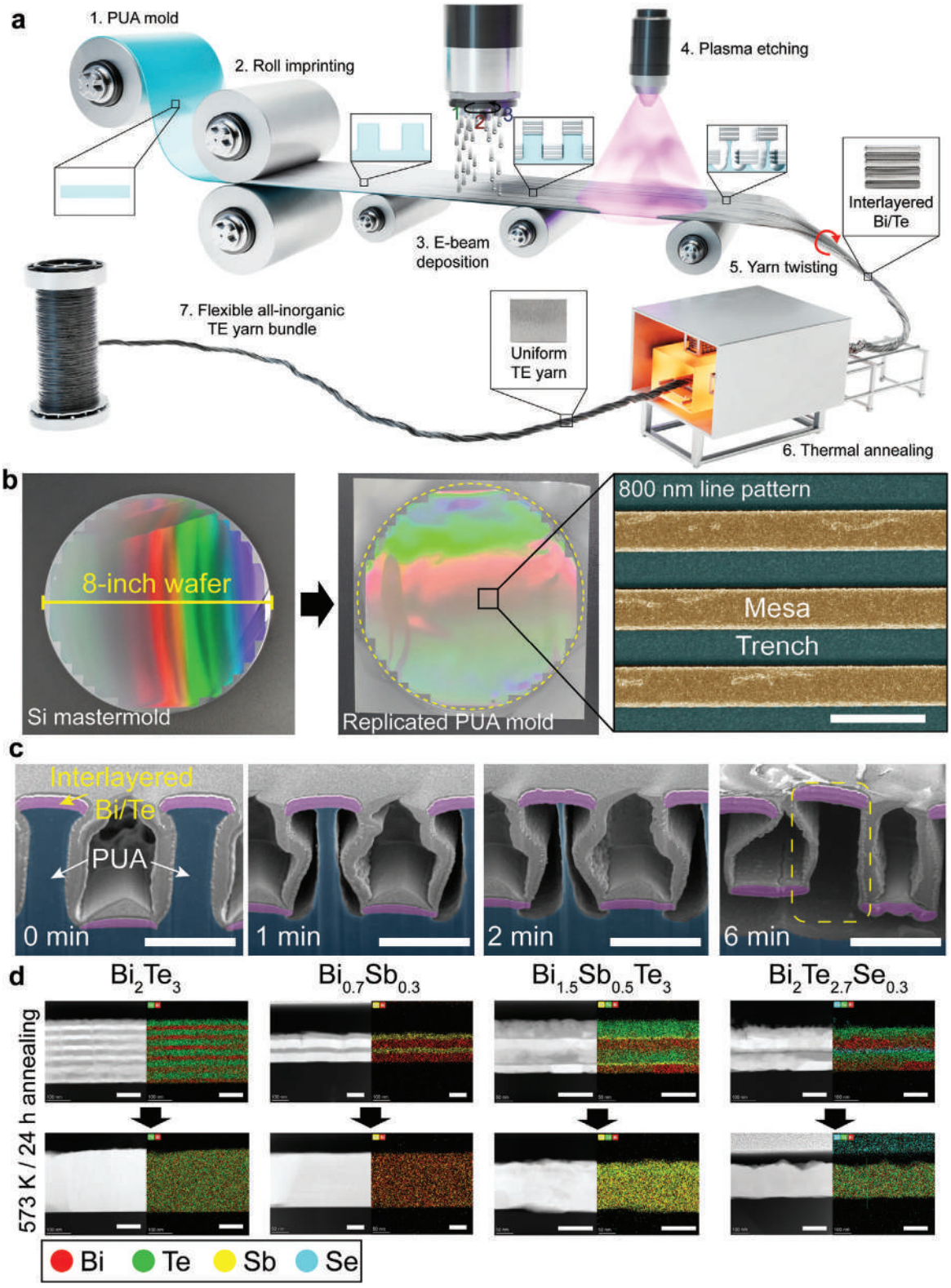


Figure 2. All-inorganic yarn fabrication process a) Schematic representation of the fabrication process for all-inorganic TE yarn. b) Photographic depiction of a nanopatterned Si master mold and a nanoimprinted PUA mold (Step a.2) alongside an enlarged colored SEM image. c) Cross-sectional SEM images of interlayered Bi/Te deposited on PUA mold after different plasma-assisted etching periods (Step a.4). d) HAADF-STEM images and corresponding STEM-EDS elemental mapping results showing versatile interlayered structures deposited on PUA mold, including Bi, Te, Sb, and Se atoms, both pre- and post-annealing for the formation of alloyed compounds (Step a.6). Scale bar, 2 μm (b), 1 μm (c), 100 nm (d).

© 2024 Wiley-VCH GmbH

15214095, 2024, 47, Downloaded from https://onlinelibrary.wiley.com/doi/10.1002/adma.202408320 by Korea University Medical Library, Wiley Online Library on [27/11/2024]. See the Terms and Conditions (https://onlinelibrary.wiley.com/terms-and-conditions) on Wiley Online Library for rules of use; OA articles are governed by the applicable Creative Commons License

to acquire the images because of their high sensitivity to generate atomic number contrast but relatively robust to other factors that affect contrast (e.g., thickness and strain).[19] Briefly, heavy elements appear brighter than lighter elements in HAADF-STEM images, serving as an excellent technique for analyzing nanoscale chemical homogeneity. We did not observe the formation of secondary phases or voids after annealing in the HAADF-STEM images. This is consistent with the results of energy-dispersive X-ray spectroscopy (EDS) elemental mapping, which shows the homogeneous mixing of constituent elements. Additional detailed procedures for TE yarn fabrication are provided in the Methods section.

2.2. Ensuring Compositional Homogeneity in TE Yarn Through Thermal Treatment

We conducted a systematic investigation into the effect of thermal annealing of Bi/Te interlayered nanoribbons on the chemical homogeneity of the fabricated TE yarn. **Figure 3a** shows the scanning electron microscopy (SEM) image of the Bi/Te interlayered nanoribbon bundles before annealing. It can be observed that several nanoribbons are well suspended without cracks or structural damage, indicating excellent flexibility of the nanoribbons. The layered structure of the interlayered nanoribbons was analyzed using backscattered electron (BSE) detectors equipped in the SEM for better visualization of the chemical contrast along the thickness direction (Figure 3b). We confirmed that the Bi and Te layers in the interlayered structure are uniformly deposited by STEM-EDS quantification, where the experimentally determined thickness of Bi and Te layers are 22 ± 2.9 and 28 ± 7.8 nm, respectively (Figure 3c). As mentioned above, we deliberately adjusted the Bi:Te thickness ratio to 2:3 based on a first-order approximation that the stoichiometry of the nanoribbon after thermal annealing predominantly depends on the mass of the film.

Thermal annealing was then performed at 573 K to promote the diffusion of Bi and Te. According to our experiments, this temperature is high enough to promote the chemical reaction but moderate enough to prevent the evaporation of volatile elements (e.g., Sb, Se, or Te). After 6 h of annealing, an island-like surface morphology can be observed resulting from the thermal diffusion of Bi and Te (Figure 3d). This characteristic structure results from the solid-state dewetting of Bi and Te at high temperatures because of the differences in their diffusion coefficients.[20] The chemical reaction was completed after 24 h of annealing, which showed a uniform contrast from the homogeneous distribution of constituent elements in the BSE image (Figure 3e). The resulting composition of the Bi/Te interlayered nanoribbon after annealing is $Bi_2Te_{3.17}$, which is in a slightly Te-excess thermodynamic condition (Figure 3f). We will later show that the determined stoichiometry is reasonable given the n-type charge transport of the TE yarn. The compositional tunability to tune the stoichiometry by adjusting the deposition thickness was confirmed by increasing the thickness of Bi layers (Figure S10, Supporting Information). EDS elemental quantification of Bi-rich sample revealed that the composition of the Bi-rich sample after thermal annealing was nearly $Bi_{0.497}Te_{0.503}$, which is in a Bi-rich thermodynamic condition compared to Bi_2Te_3. Furthermore, the original thickness (≈300 nm) was well preserved, indicating that the volatilization of the constituent elements was not significant under these process conditions. We systematically studied and summarized the effect of annealing temperature and time, which can be found in Supporting Information.

To analyze the change in bonding characteristics after thermal annealing, X-ray photoelectron spectroscopy (XPS) analysis was conducted (Figure 3g,h). The XPS spectra for Bi 4f and Te 3d orbitals showed an obvious peak shift to the higher and lower binding energy, respectively. The thermochemical electronegativities of Bi and Te are 2.69 and 3.14, respectively.[21] Therefore, electrons tend to transfer from Bi to Te during the chemical reaction, and Te should exhibit lower binding energies due to the screening effect.[22] Both Bi and Te existed in the metallic state before annealing, showing peak positions at 162.3 and 572.5 eV, respectively.[23] However, their peak positions shifted to 162.6 and 572.0 eV after annealing, corresponding to those of Bi^{3+} and Te^{2-}, respectively.[24] With a negligible amount of Bi_2O_3 or TeO_2 detected, these observations suggest the successful formation of Bi_2Te_3 without significant oxidation during thermal annealing. Raman spectra were also obtained to study the change in vibrational modes (Figure 3i). Metallic Bi has a crystal structure of *R*-3*m* (same as Bi_2Te_3) and exhibits 2 distinct Raman active modes, E_g (69 cm^{-1}) and A_{1g} (96 cm^{-1}).[25] However, neither of these peaks was observed before annealing, and we assume that the Raman signal of Bi layers is mostly blocked by the highly reflective Te layer on top. Indeed, 2 Raman peaks of Te were observed at 123 and 140 cm^{-1}, corresponding to A_{1u} and E_2 modes, respectively.[26] After annealing, 2 new peaks appear at 61 and 102 cm^{-1} can be indexed to $A^1{}_{1g}$ and $E^2{}_g$ of the Bi_2Te_3 lattice, which do not overlap with signals from Te. The formation of the Bi_2Te_3 phase is also confirmed by X-ray diffraction (XRD) analysis (Figure 3j).

Finally, we characterized the Seebeck coefficient of the TE yarn post-annealing using a custom-built Seebeck coefficient measurement setup (Figure 3k). The TE yarn was suspended between the 2 Peltier devices using Ag paste and carbon tape. Then, a temperature gradient was created by simultaneously operating the 2 Peltier devices. Here, one device was inverted with the cold side facing downward (opposite to the TE yarn) and operated as a Joule heater, while the other device continuously cooled the TE yarn. Temperature was continuously monitored using K-type thermocouples. The measured TE voltage as a function of the temperature difference is shown in Figure 3l. The relative Seebeck coefficient was calculated from the slope of the TE voltage and the temperature difference, yielding a value of −126.6 μV K^{-1}. Although the magnitude of the Seebeck coefficient largely depends on the carrier concentration, the measured value is reasonable considering that bulk n-type Bi_2Te_3 typically exhibits a Seebeck coefficient ranging from −100 to −200 μV K^{-1}.[27] The negative sign of the Seebeck coefficient indicates that the Bi_2Te_3 yarn is an n-type semiconductor. In the Te-excess thermodynamic state, the formation of donor-like Te-on-Bi antisite defects (Te_{Bi}) is favored.[28] Therefore, the observed negative sign is consistent with the compositional analysis results. Overall, we confirmed the formation of a homogeneous Bi_2Te_3 phase by thermal annealing of the Bi/Te interlayered nanoribbon and demonstrated the voltage

© 2024 Wiley-VCH GmbH

15214095, 2024, 47, Downloaded from https://onlinelibrary.wiley.com/doi/10.1002/adma.202408320 by Korea University Medical Library, Wiley Online Library on [27/11/2024]. See the Terms and Conditions (https://onlinelibrary.wiley.com/terms-and-conditions) on Wiley Online Library for rules of use; OA articles are governed by the applicable Creative Commons License

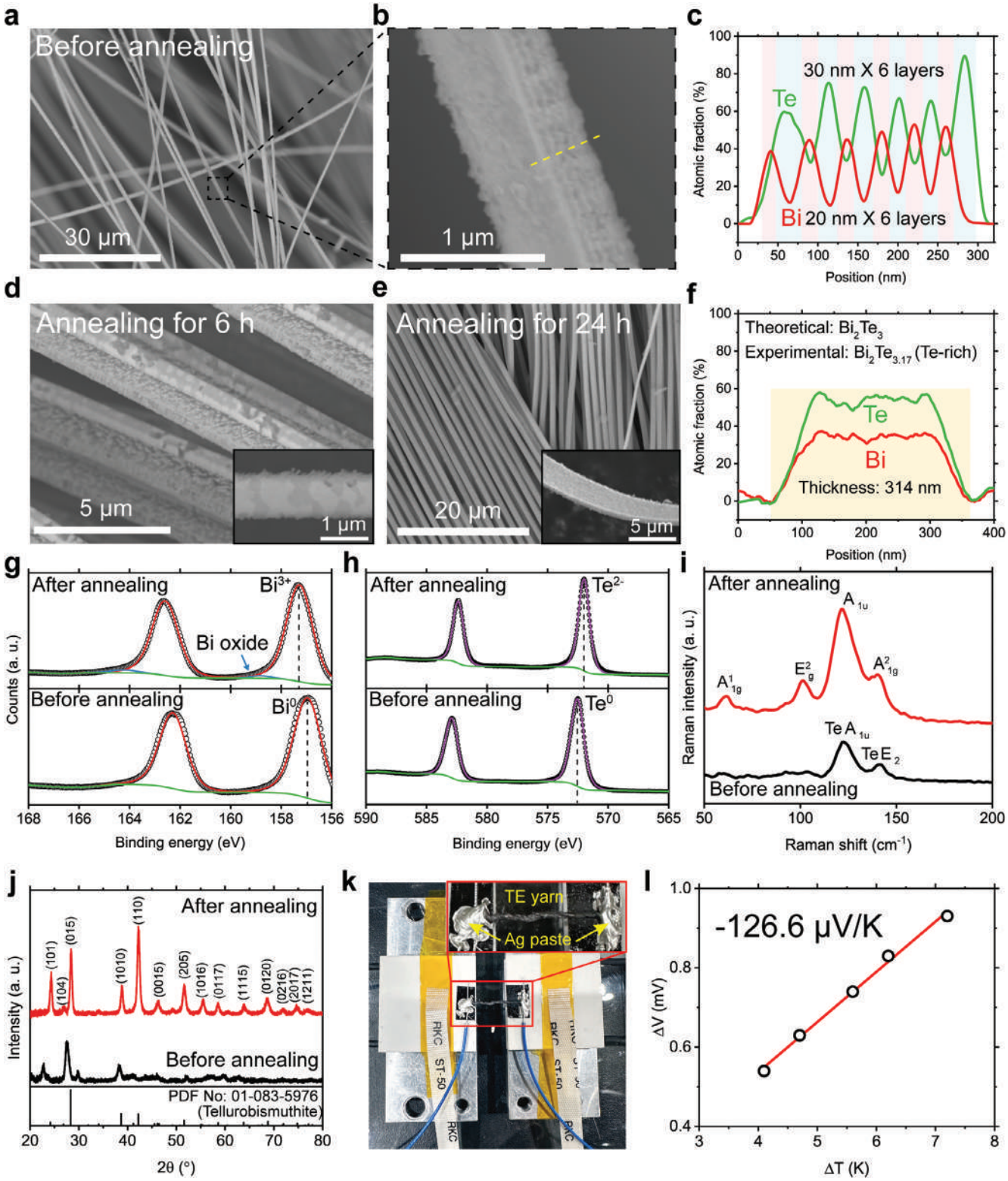


Figure 3. Material characterization of TE yarn. a, d, e) BSE images of Bi/Te interlayered nanoribbon: (a) before annealing, (d) after 6 h annealing, and (e) after 24 h annealing. SEM images in b) and insets in (d) and (e) show magnified images of a single nanoribbon. c) EDS elemental quantification results along the yellow line denoted in (b). f) EDS elemental quantification after 24 h annealing. g, h) XPS spectra, i) Raman spectra, and j) XRD pattern of the TE yarn before and after annealing. k) Digital photograph of the experimental setup for measuring the Seebeck coefficient of the TE yarn. l) Measured TE voltage versus temperature difference of the TE yarn.

© 2024 Wiley-VCH GmbH

15214095, 2024, 47, Downloaded from https://onlinelibrary.wiley.com/doi/10.1002/adma.202408320 by Korea University Medical Library, Wiley Online Library on [27/11/2024]. See the Terms and Conditions (https://onlinelibrary.wiley.com/terms-and-conditions) on Wiley Online Library for rules of use; OA articles are governed by the applicable Creative Commons License

generation capability of the fabricated TE yarn under the temperature gradient.

2.3. Electromechanical Characterization of the TE Yarn

To further explore the capabilities of our TE yarn, we conducted electromechanical property tests. Three types of experiments were performed: a bending test (**Figure** 4a–c), a strain test (Figure 4d–f), and an extreme temperature condition test (Figure 4g). Each test aimed to investigate the flexibility, stretchability, and adaptability of the yarn under extreme conditions. The experimental setup for each test is described in Supporting Information (Figure S1, Supporting Information). During the bending and strain tests, electrical characteristics were monitored by measuring electrical resistance. Detailed experimental conditions and procedures can be found in the Methods section.

First, the bending test was conducted within a curvature range of 0 to 0.49 mm^{-1}, revealing a maximum electrical resistance change of 4.2% (Figure 4a). The shape of the yarn at various curvature ranges is depicted in Figure 4b. The observed changes in resistance can be attributed to the internal contact between nanoribbons, leading to their relocation. To assess reliability, a cyclic bending test was performed for 1000 cycles within the same curvature range. The results showed a maximum resistance change of 2.3% ($\Delta R/R_0 = 0.023$), indicating no noticeable change in electrical properties during the test (Figure 4c). Therefore, the TE yarn demonstrated flexibility, tolerating bending up to a curvature of ≈0.5 mm^{-1} without noticeable changes in electrical characteristics. In contrast, when attempting a 3-point flexural test on bulk Bi_2Te_3 (details in the Supporting Information), the sample broke at an immeasurably small curvature, highlighting a significant improvement in flexibility achieved by morphing the material into a nanoribbon yarn (Figure S2, Supporting Information).

Next, a strain test was performed to assess the stretchability of the TE yarn. The test covered a strain range of 0% to 14.5%. The results revealed that the TE yarn remains electrically stable up to ≈5% strain ($\Delta R/R_0 = 0.01$). However, at 14.5% strain, the resistance increased by 12.3 times compared to the initial value (Figure 4d). The minute electrical resistance changes observed at strains below 5% are likely attributable to the yarn's structure. During the initial twisting of aligned nanofibers, a compressive pre-strain of 5%–10% is applied to prevent possible deformation and subsequent breakage of the nanofibers. This pre-compressed length serves as a buffer against stretch after the yarn is formed, preventing the nanofibers from fracturing in the early stages of deformation. Beyond 5% strain, the resistance exhibits an exponential increase. This tendency can be attributed to the formation of internal microcracks during stretching, a common phenomenon in brittle materials undergoing deformation.[29]

The Seebeck coefficient remained stable up to a strain of $\varepsilon = 10\%$ under the same measurement conditions, exceeding the strain threshold of 5% observed for electrical resistance. Theoretically, for a homogeneous material under the single parabolic band approximation at a given reduced Fermi level, η, the Seebeck coefficient (S) and the electrical conductivity (σ) are described as follows:

$$S = \frac{k_B}{e}\left(\frac{2F_1(\eta)}{F_0(\eta)} - \eta\right) \tag{2}$$

$$\sigma = \mu_0 e\frac{\left(2m_D^* k_B T\right)^{\frac{3}{2}}}{6\pi^2\hbar^3}\frac{F_{1/2}(\eta)\,F_{-1/2}(\eta)}{F_0(\eta)} \tag{3}$$

where e, k_B, T, $\hbar$, m_D^*, μ_0, and $F_j(\eta)$ represents the elementary charge, Boltzmann constant, absolute temperature, reduced Planck constant, density-of-states effective mass, mobility free parameter, and the j-th order Fermi integral, respectively. If the change in electrical conductivity with the applied tensile strain is due to the variation of η, it should be directly associated with the change in the Seebeck coefficient. However, cracks and voids formed during elongation can directly reduce the mean free path of charge carriers, leading to lower μ_0 values after tensile testing. Consequently, the applied strain would only decrease σ while maintaining S.

Although the transport equations above can explain the different responses of S and σ to tensile strain, they do not account for the decrease in the magnitude of the Seebeck coefficient with applied strain above 12%. To address this, we need to consider the characteristics of fibrillar TE materials. Detailed analysis of the 3D internal structure of the Bi_2Te_3 yarn using X-ray tomography revealed that several nanoribbon clusters form junctions with neighboring clusters (Figure S13, Supporting Information). This suggests that the electrical and heat current would flow in the parallel circuit consisting of the nanoribbon clusters and their junctions, implying that the disconnection process during elongation contributes additional resistance to this system.

Accordingly, we define the connectivity factor (φ) ranging from 0 to 1 as a variable that monotonically decreases during elongation. The total Seebeck coefficient (S_{tot}) and electrical conductivity (σ_{tot}) are then given by:

$$S_{tot} = \frac{1}{\sigma_{junction}(1-\varphi) + \sigma_{cluster}\varphi}\left[S_{junction}(1-\varphi)\,\sigma_{junction} + S_{cluster}\varphi\sigma_{cluster}\right] \tag{4}$$

$$\sigma_{tot} = \sigma_{junction}\,(1-\varphi) + \sigma_{cluster}\varphi \tag{5}$$

where $\sigma_{junction}$, $\sigma_{cluster}$, $S_{junction}$, and $S_{cluster}$ Denote the electrical conductivity and Seebeck coefficient of the junction and cluster, respectively. Using this model, we calculated the theoretical Seebeck coefficient and electrical conductivity, achieving satisfactory agreement with the experimental data (Figure S14, Supporting Information). However, a significant increase in electrical resistance deviates from the model, suggesting the formation of additional resistance components such as cracks and voids with the applied tensile strain. Furthermore, the change in the Seebeck coefficient under tensile strain is found to be less abrupt. This may be due to the nature of the Seebeck effect, where the open-circuit voltage largely depends on the temperature gradient rather than the internal resistance. Consequently, we observe different strain responses in electrical resistances and Seebeck coefficient measurements.

The shape of the yarn at each strain is depicted in Figure 4e. The inset images show SEM images of the yarn morphology at corresponding strains. It is evident that as the strain increases, the surface angle of twist decreases ($\theta = 49.0°$ at $\varepsilon = 0\%$ and

© 2024 Wiley-VCH GmbH

15214095, 2024, 47, Downloaded from https://onlinelibrary.wiley.com/doi/10.1002/adma.202408320 by Korea University Medical Library, Wiley Online Library on [27/11/2024]. See the Terms and Conditions (https://onlinelibrary.wiley.com/terms-and-conditions) on Wiley Online Library for rules of use; OA articles are governed by the applicable Creative Commons License

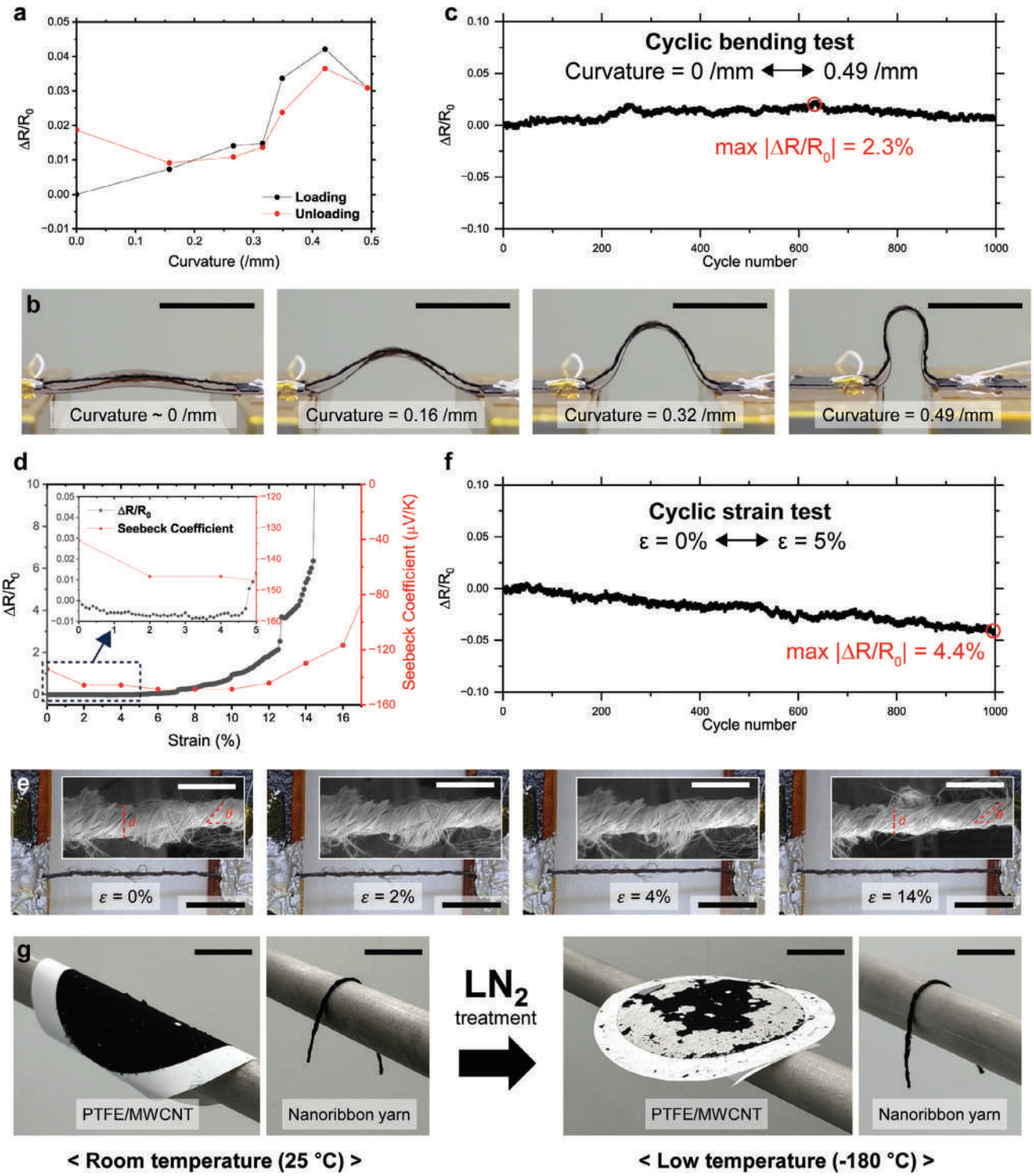


Figure 4. Electromechanical characterization of the TE yarn. a) Bending test results. The sample exhibits minute change within the bending curvature range of 0 to 0.49 mm^{-1}, confirming its flexibility. b) Photographic images of the bending test with various curvatures. Scale bars, 1 cm. c) Results of cyclic bending test. The sample shows minute change during the test, confirming its reliability within the curvature range of 0–0.49 mm^{-1}. d) Results of the strain test. The sample shows minute resistance change (≈1%) up to 5% strain and starts to increase afterward. (Inset) Magnified result for strain below 5%. e) Photographic images of the strain test result. Scale bars, 5 mm. (Inset) SEM image of strain test results. Scale bars, 1 mm. f) Results of the cyclic strain test. The sample shows minute resistance change during the test, confirming its reliability within the strain range of 0% to 5%. g) Results of the extreme temperature condition test. While the PTFE/MWCNT samples fail after exposure to cryogenic conditions, the proposed TE material-based TE yarn maintains its flexibility and morphology under cryogenic conditions. Scale bars, 2 cm.

© 2024 Wiley-VCH GmbH

15214095, 2024, 47, Downloaded from https://onlinelibrary.wiley.com/doi/10.1002/adma.202408320 by Korea University Medical Library, Wiley Online Library on [27/11/2024]. See the Terms and Conditions (https://onlinelibrary.wiley.com/terms-and-conditions) on Wiley Online Library for rules of use; OA articles are governed by the applicable Creative Commons License

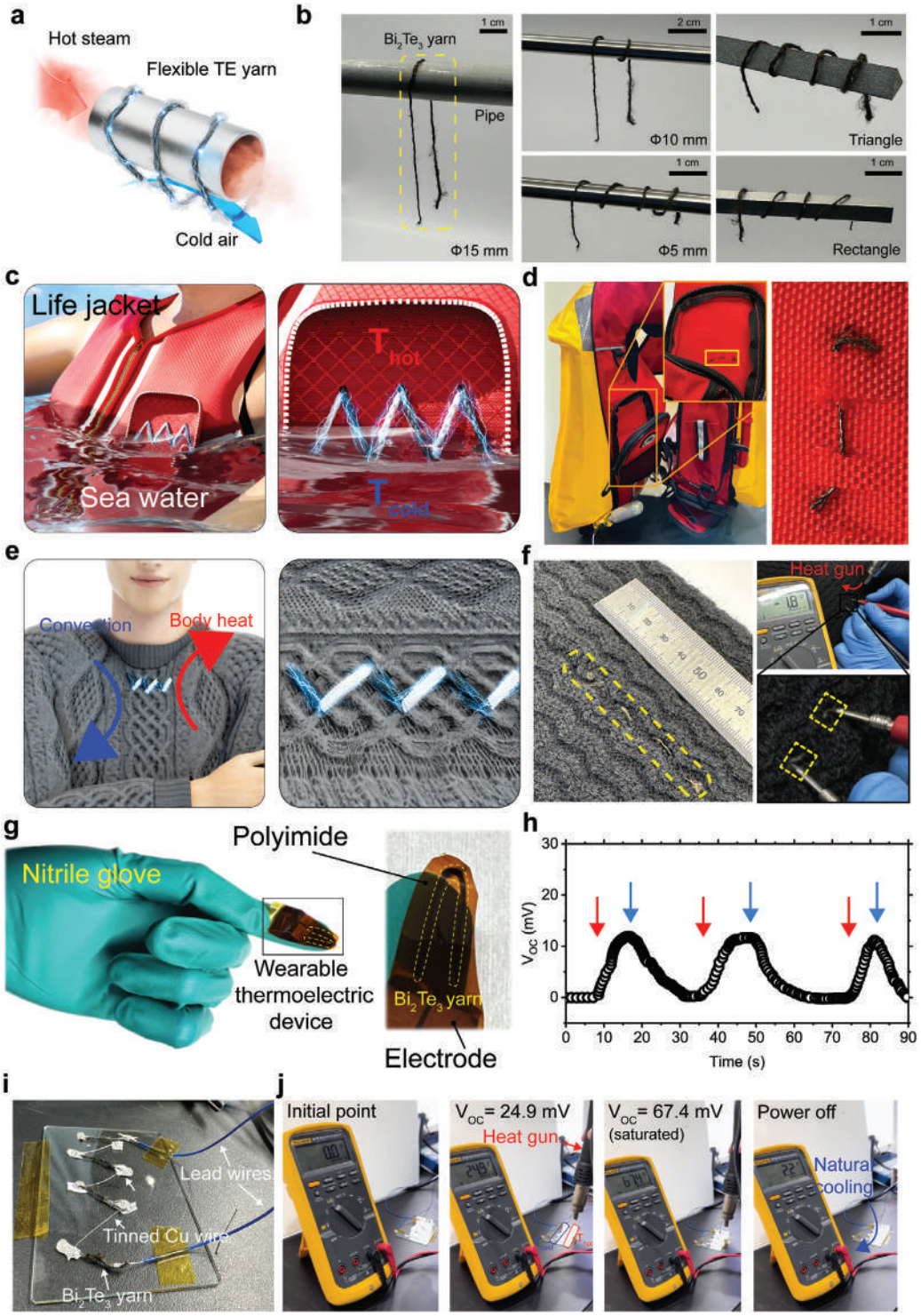


Figure 5. Prospective applications for leveraging the intrinsic flexibility of TE yarns. a) A schematic illustration depicting the energy harvesting scenario exploiting the temperature differential between the hot fluid inside a pipe and the colder external air. b) Photographic images showcasing Bi_2Te_3 yarn suspended and coiled around metallic pipes of various dimensions and shapes. c) A schematic illustration depicting the energy harvesting scenario leveraging the temperature contrast between a warm human body and cold seawater. d) Photographic images demonstrating Bi_2Te_3 yarn integrated into a life jacket through knitting. e) A schematic illustration illustrating the energy harvesting scenario utilizing the temperature disparity between a warm human body and the surrounding cold air. f) Photographic images exhibiting Bi_2Te_3 yarn incorporated into a sweater through knitting. g) Digital photograph of the wearable TE device with the Bi_2Te_3 yarn. h) Time-dependent open circuit voltage (V_{OC}) of the wearable TE generator in g). Red and blue arrows indicate the points where the TE generator is attached to and detached from the hot surface, respectively. i) Photographic image of a 4-pair TE generator consisting of Bi_2Te_3 yarns and tinned copper wires. j) Photographic images showing TE voltage generation upon heating with a heat gun.

© 2024 Wiley-VCH GmbH

15214095, 2024, 47, Downloaded from https://onlinelibrary.wiley.com/doi/10.1002/adma.202408320 by Korea University Medical Library, Wiley Online Library on [27/11/2024]. See the Terms and Conditions (https://onlinelibrary.wiley.com/terms-and-conditions) on Wiley Online Library for rules of use; OA articles are governed by the applicable Creative Commons License

$\theta = 38.8°$ at $\varepsilon = 14\%$) and the diameter decreases ($d = 510\ \mu m$ at $\varepsilon = 0\%$ and $d = 410\ \mu m$ at $\varepsilon = 14\%$). To assess reliability, a cyclic strain test was conducted within the stable strain range of 0% to 5% for 1000 cycles. The results revealed the maximum electrical resistance change of 4.4% during the test (Figure 4f). The continuous decrease in electrical resistance observed during the test may be attributed to the relocation of nanoribbons within the nano yarn during strain, stabilizing their positions. In conclusion, the morphology of the TE yarn provides both mechanical flexibility and stretchability to the inherently brittle TE materials.

Lastly, to assess the feasibility of flexible TE yarn under extreme temperature conditions, a comparison was made between polymer binder-based TE materials (PBTE) and TE yarn. Here, we chose carbon nanotube composites as a representative PBTE, which has been successful in providing both moderate flexibility and TE properties in an ambient condition.[18c,30] PBTE, represented by multi-walled carbon nanotubes (MWCNTs) coated on a poly(tetrafluoroethylene) (PTFE) filter (PTFE/MWCNT), and TE yarn (Bi_2Te_3-based yarn) were exposed to a cryogenic environment (Liquid nitrogen (LN_2)) and then bent. The results showed that PTFE/MWCNT lost its flexibility and the dispersed CNTs were fractured, while the TE yarn maintained a similar level of flexibility as before (Figure 4g). In contrast to PBTE, which relies on polymer binders and is limited by the properties of the polymer itself, all-inorganic TE yarns can still be utilized under cryogenic environments. This advantage makes them more practical for applications requiring TE materials in extreme temperatures, such as radioisotope TE generators in space[31] and cryogenic TE generation.[32] As the demand for TE materials in cryogenic environments increases, the availability of all-inorganic TE yarns offers a more reliable solution compared to PBTE.

2.4. Prospective Applications of the TE Yarns

We propose potential application scenarios and a pn-junction TE system to leverage the flexibility of our TE yarn. First, the developed flexible Bi_2Te_3 yarn exhibited potential for energy harvesting by exploiting the temperature gradient between the hot fluid within a pipe and the cooler external air, as depicted in **Figure 5a**. Thanks to its remarkable flexibility, the yarn can be seamlessly suspended and even coiled around various metallic pipes with arbitrary dimensions. Figure 5b illustrates the successful integration of the Bi_2Te_3 yarn onto circular pipes with diameters of 5, 10, and 15 mm, as well as triangular and square pipes with a hypotenuse of 5 mm. Second, the yarn can find diverse applications in energy harvesting devices leveraging the temperature disparity between a human body and cold seawater, as illustrated in Figure 5c,d. Integration into life jackets via knitting enables potential electrical energy generation during emergencies at sea, potentially powering intelligent life jackets equipped with GPS sensors.[33] Lastly, the yarn can be incorporated into commercial sweaters for daily energy harvesting purposes, utilizing the temperature difference between a human body and the surrounding cold air, as shown in Figure 5e,f. The yarn's low stiffness, high flexibility, and stretchability not only facilitate unrestricted movement but also enhance mechanical stability against complex deformations when integrated into clothing and worn by individuals. The simple TE device comprising a Bi_2Te_3 yarn and electrode passivated with polyimide, successfully generated an open circuit voltage (V_{OC}) of 13 mV under a temperature gradient (Figure 5g,h). While the response time and the recovery time varied slightly in each trial, the maximum V_{OC} and the overall behavior were similar and repeatable.

Finally, we confirmed the energy harvesting capability of the developed TE yarn by fabricating a simple 4-pair TE generator composed of Bi_2Te_3 yarn and tinned Cu wire as an n-, and p-type TE element, respectively (Figure 5i). As shown in Figure 5j, any voltage generation was not observed under a thermal equilibrium. However, the TE device delivered an open circuit voltage (V_{OC}) of 24.9 mV when the bottom side of the TE device was heated with a heat gun, and the maximum V_{OC} of the device was measured to be 67.4 mV. The output voltage of the device slowly decreased when the heat gun was turned off and the device was left to be cooled by natural convection. This means that the measured voltage indeed resulted from the temperature gradient and Seebeck effect of the TE device.

3. Conclusion

In the present study, we have demonstrated that the nanoscale flexibility can be extended macroscopically via twisting all-inorganic nanoribbons into yarn structures, developing structurally flexible TE energy harvesters. The process developed in this work has further expanded the horizon of TE material synthesis, enabling the controlled fabrication of multiple all-inorganic TE compounds from elemental components with unprecedented flexibility. The developed TE yarn showed a minute resistance change under bending curvature of 0.5 mm^{-1} and tensile strain of 5% over 1000 cycles, confirming its excellent mechanical properties. Moreover, the TE yarn can be freely wound around metal tubes, embedded in a life jacket, or knitted into a sweater, opening up new possibilities for TE materials as wearable and flexible energy harvesters for future self-powered device applications. While we have mainly focused on Bi_2Te_3-based compounds in this work, we are optimistic about the potential to adapt our methodology to several state-of-the-art TE materials (e.g., $CoSb_3$, SnSe, $AgSbTe_2$, and SiGe). These materials could be fashioned into yarn structures and are poised to excel in niche applications beyond high-temperature power generation. Furthermore, it presents a fascinating opportunity to create flexible yet functional yarns from inherently brittle inorganic compounds such as ferroelectric and magnetic materials, thereby overcoming their traditional limitations of brittleness.

Supporting Information

Supporting Information is available from the Wiley Online Library or from the author.

Acknowledgements

H.J., J.A., and Y.J. contributed equally to this work. This work was supported by the Alchemist Project grant funded by the Korea Evaluation Institute of Industrial Technology (KEIT) and the Korea Government (MOTIE) (Project Number: 1415179744, 20019169), by Korea Evaluation Institute of Industrial Technology (KEIT) grant funded by the Korea government (MOTIE, Grant No. RS-2022-00154781, Development of large-area

© 2024 Wiley-VCH GmbH

15214095, 2024, 47, Downloaded from https://onlinelibrary.wiley.com/doi/10.1002/adma.202408320 by Korea University Medical Library, Wiley Online Library on [27/11/2024]. See the Terms and Conditions (https://onlinelibrary.wiley.com/terms-and-conditions) on Wiley Online Library for rules of use; OA articles are governed by the applicable Creative Commons License

wafer-level flexible/stretchable hybrid sensor platform technology for form factor-free highly integrated convergence sensor), and by the National Research Foundation of Korea (NRF) grant funded by the Korean government (MSIT) [No. 2020M3D1A1110501, 2021R1A2C3008742, and RS-2024-00406240].

Conflict of Interest

The authors declare no conflict of interest.

Data Availability Statement

The data that support the findings of this study are available from the corresponding author upon reasonable request.

Keywords

all-inorganic, flexible, mechanical properties, thermoelectrics, yarns

Received: June 11, 2024
Revised: September 2, 2024
Published online: September 17, 2024

[1] a) B. Y. Ahn, E. B. Duoss, M. J. Motala, X. Guo, S.-I. Park, Y. Xiong, J. Yoon, R. G. Nuzzo, J. A. Rogers, J. A. Lewis, *Science* **2009**, *323*, 1590; b) J. Yoon, A. J. Baca, S.-I. Park, P. Elvikis, J. B. Geddes, L. Li, R. H. Kim, J. Xiao, S. Wang, T.-H. Kim, M. J. Motala, B. Y. Ahn, E. B. Duoss, J. A. Lewis, R. G. Nuzzo, P. M. Ferreira, Y. Huang, A. Rockett, J. A. Rogers, *Nat. Mater.* **2008**, *7*, 907; c) B. C. K. Tee, C. Wang, R. Allen, Z. Bao, *Nat. Nanotechnol.* **2012**, *7*, 825.

[2] a) W. Lee, H. Kim, I. Kang, H. Park, J. Jung, H. Lee, H. Park, J. S. Park, J. M. Yuk, S. Ryu, J.-W. Jeong, J. Kang, *Science* **2022**, *378*, 637; b) M. Amjadi, A. Pichitpajongkit, S. Lee, S. Ryu, I. Park, *ACS Nano* **2014**, *8*, 5154.

[3] F. Bouville, E. Maire, S. Meille, B. Van de Moortèle, A. J. Stevenson, S. Deville, *Nat. Mater.* **2014**, *13*, 508.

[4] a) B. Lee, H. Cho, K. T. Park, J.-S. Kim, M. Park, H. Kim, Y. Hong, S. Chung, *Nat. Commun.* **2020**, *11*, 5948; b) S. J. Kim, H. E. Lee, H. Choi, Y. Kim, J. H. We, J. S. Shin, K. J. Lee, B. J. Cho, *ACS Nano* **2016**, *10*, 10851; c) J. W. Park, C. S. Kim, H. Choi, Y. J. Kim, G. S. Lee, B. J. Cho, *Adv. Mater. Technol.* **2020**, *5*, 2000486.

[5] S. Wu, J. Zhang, R. B. Ladani, A. R. Ravindran, A. P. Mouritz, A. J. Kinloch, C. H. Wang, *ACS Appl. Mater. Interfaces* **2017**, *9*, 14207.

[6] G. Zhang, Y. Sun, B. Qian, H. Gao, D. Zuo, *Polym. Test.* **2020**, *90*, 106670.

[7] S. Wang, T. Xie, H. Xie, *Appl. Therm. Eng.* **2018**, *130*, 847.

[8] a) A. El-Desouky, M. Carter, M. A. Andre, P. M. Bardet, S. LeBlanc, *Mater. Lett.* **2016**, *185*, 598; b) P. Qiu, T. Mao, Z. Huang, X. Xia, J. Liao, M. T. Agne, M. Gu, Q. Zhang, D. Ren, S. Bai, *Joule* **2019**, *3*, 1538; c) Z. Bu, X. Zhang, Y. Hu, Z. Chen, S. Lin, W. Li, Y. Pei, *Energy Environ. Sci.* **2021**, *14*, 6506.

[9] a) Y. Du, J. Y. Xu, B. Paul, P. Eklund, *Appl. Mater. Today* **2018**, *12*, 366; b) Y. Wang, L. Yang, X. L. Shi, X. Shi, L. Chen, M. S. Dargusch, J. Zou, Z. G. Chen, *Adv. Mater.* **2019**, *31*, 1807916.

[10] S. Hwang, D. Jang, B. Lee, Y.-S. Ryu, J. Kwak, H. Kim, S. Chung, *Adv. Energy Mater.* **2023**, *13*, 2204171.

[11] a) F. Kim, S. E. Yang, H. Ju, S. Choo, J. Lee, G. Kim, S.-h. Jung, S. Kim, C. Cha, K. T. Kim, S. Ahn, H. G. Chae, J. S. Son, *Nat. Electron.* **2021**, *4*, 579; b) J. Lee, S. Choo, H. Ju, J. Hong, S. E. Yang, F. Kim, D. H. Gu, J. Jang, G. Kim, S. Ahn, J. E. Lee, S. Y. Kim, H. G. Chae, J. S. Son, *Adv. Energy Mater.* **2021**, *11*, 2100190; c) F. Kim, B. Kwon, Y. Eom, J. E. Lee, S. Park, S. Jo, S. H. Park, B.-S. Kim, H. J. Im, M. H. Lee, T. S. Min, K. T. Kim, H. G. Chae, W. P. King, J. S. Son, *Nat. Energy* **2018**, *3*, 301.

[12] a) X. Shi, H. Chen, F. Hao, R. Liu, T. Wang, P. Qiu, U. Burkhardt, Y. Grin, L. Chen, *Nat. Mater.* **2018**, *17*, 421; b) Q. Yang, S. Yang, P. Qiu, L. Peng, T.-R. Wei, Z. Zhang, X. Shi, L. Chen, *Science* **2022**, *377*, 854; c) J. Liang, T. Wang, P. Qiu, S. Yang, C. Ming, H. Chen, Q. Song, K. Zhao, T.-R. Wei, D. Ren, Y.-Y. Sun, X. Shi, J. He, L. Chen, *Energy Environ. Sci.* **2019**, *12*, 2983; d) S. He, Y. Li, L. Liu, Y. Jiang, J. Feng, W. Zhu, J. Zhang, Z. Dong, Y. Deng, J. Luo, W. Zhang, G. Chen, *Sci. Adv.* **2020**, *6*, eaaz8423; e) K. Shen, Q. Yang, P. Qiu, Z. Zhou, S. Yang, T.-R. Wei, X. Shi, *Adv. Mater.* 2407424.

[13] a) Z. Gao, T.-R. Wei, T. Deng, P. Qiu, W. Xu, Y. Wang, L. Chen, X. Shi, *Nat. Commun.* **2022**, *13*, 7491; b) T.-R. Wei, M. Jin, Y. Wang, H. Chen, Z. Gao, K. Zhao, P. Qiu, Z. Shan, J. Jiang, R. Li, L. Chen, J. He, X. Shi, *Science* **2020**, *369*, 542; c) T. Deng, Z. Gao, P. Qiu, T.-R. Wei, J. Xiao, G. Wang, L. Chen, X. Shi, *Adv. Sci.* **2022**, *9*, 2203436; d) T. Deng, Z. Gao, P. Qiu, Z. Zhou, C. Ming, Z. Liu, Z. Li, S. Yang, T.-R. Wei, G. Wang, L. Chen, X. Shi, *Adv. Mater.* **2024**, *36*, 2304219.

[14] J. Peng, G. J. Snyder, *Science* **2019**, *366*, 690.

[15] C. Yang, D. Souchay, M. Kneiss, M. Bogner, H. M. Wei, M. Lorenz, O. Oeckler, G. Benstetter, Y. Q. Fu, M. Grundmann, *Nat. Commun.* **2017**, *8*, 16076.

[16] a) B. Xin, A. L.e Febvrier, J. Lu, B. Paul, P. Eklund, *Nanoscale Adv.* **2022**, *4*, 3318; b) B. Xin, B. Paul, A. le Febvrier, P. Eklund, *Mater. Sci. Semicond. Process* **2023**, *156*, 107300; c) B. Paul, J. Lu, P. Eklund, *ACS Appl. Mater. Interfaces* **2017**, *9*, 25308; d) B. Paul, E. M. Björk, A. Kumar, J. Lu, P. Eklund, *ACS Appl. Energy Mater.* **2018**, *1*, 2261; e) B. Xin, L. Wang, A. L.e Febvrier, A. Elsukova, B. Paul, N. Solin, P. Eklund, *ACS Omega* **2022**, *7*, 23988.

[17] D. Li, X. L. Shi, J. Zhu, T. Cao, X. Ma, M. Li, Z. Han, Z. Feng, Y. Chen, J. Wang, W. D. Liu, H. Zhong, S. Li, Z. G. Chen, *Nat. Commun.* **2024**, *15*, 4242.

[18] a) H. Shang, C. Dun, Y. Deng, T. Li, Z. Gao, L. Xiao, H. Gu, D. J. Singh, Z. Ren, F. Ding, *J. Mater. Chem. A* **2020**, *8*, 4552; b) H. Shang, T. Li, D. Luo, L. Yu, Q. Zou, D. Huang, L. Xiao, H. Gu, Z. Ren, F. Ding, *ACS Appl. Mater. Interfaces* **2020**, *12*, 7358; c) Q. Jin, S. Jiang, Y. Zhao, D. Wang, J. Qiu, D.-M. Tang, J. Tan, D.-M. Sun, P.-X. Hou, X.-Q. Chen, K. Tai, N. Gao, C. Liu, H.-M. Cheng, X. Jiang, *Nat. Mater.* **2019**, *18*, 62; d) H.-J. Shang, F.-Z. Ding, Y. Deng, H. Zhang, Z.-B. Dong, W.-J. Xu, D.-X. Huang, H.-W. Gu, Z.-G. Chen, *Nanoscale* **2018**, *10*, 20189.

[19] Z. Wang, Z. Li, S. Park, A. Abdela, D. Tang, R. Palmer, *Phys. Rev. B* **2011**, *84*, 073408.

[20] X. Cen, X. Zhang, A. M. Thron, K. van Benthem, *Acta Mater.* **2016**, *119*, 167.

[21] C. Tantardini, A. R. Oganov, *Nat. Commun.* **2021**, *12*, 2087.

[22] H. Jang, J. H. Park, H. S. Lee, B. Ryu, S.-D. Park, H.-A. Ju, S.-H. Yang, Y.-M. Kim, W. H. Nam, H. Wang, J. Male, G. J. Snyder, M. Kim, Y. S. Jung, M.-W. Oh, *Adv. Sci.* **2021**, *8*, 2100895.

[23] a) S. Suzer, N. Ertas, O. Y. Ataman, *Appl. Spectrosc.* **1999**, *53*, 479; b) A. B. Mandale, S. Badrinarayanan, *J. Electron Spectros. Relat. Phenomena* **1990**, *53*, 87.

[24] H. Bando, K. Koizumi, Y. Oikawa, K. Daikohara, V. Kulbachinskii, H. Ozaki, *J. Condens. Matter Phys.* **2000**, *12*, 5607.

[25] a) D. Lu, S. Luo, S. Liu, H. Yao, X. Ren, W. Zhou, D. Tang, X. Qi, J. Zhong, *J. Phys. Chem. C* **2018**, *122*, 24459; b) J. Kim, M.-W. Oh, G. Kim, J.-H. Bahk, J. Y. Song, S. G. Jeon, D. W. Chun, J.-H. Bae, W. Shim, W. Lee, *Acta Mater.* **2018**, *144*, 145.

[26] J.-K. Qin, P.-Y. Liao, M. Si, S. Gao, G. Qiu, J. Jian, Q. Wang, S.-Q. Zhang, S. Huang, A. Charnas, Y. Wang, M. J. Kim, W. Wu, X. Xu, H.-Y. Wang, L. Yang, Y. Khin Yap, P. D. Ye, *Nat. Electron.* **2020**, *3*, 141.

 © 2024 Wiley-VCH GmbH

15214095, 2024, 47, Downloaded from https://onlinelibrary.wiley.com/doi/10.1002/adma.202408320 by Korea University Medical Library, Wiley Online Library on [27/11/2024]. See the Terms and Conditions (https://onlinelibrary.wiley.com/terms-and-conditions) on Wiley Online Library for rules of use; OA articles are governed by the applicable Creative Commons License

[27] I. T. Witting, T. C. Chasapis, F. Ricci, M. Peters, N. A. Heinz, G. Hautier, G. J. Snyder, *Adv. Electron. Mater.* **2019**, *5*, 1800904.
[28] a) A. Hashibon, C. Elsässer, *Phys. Rev. B* **2011**, *84*, 144117; b) M. W. Oh, J. H. Son, B. S. Kim, S. D. Park, B. K. Min, H. W. Lee, *J. Appl. Phys.* **2014**, 115.
[29] a) T. Sujidkul, C. E. Smith, Z. Ma, G. N. Morscher, Z. Xia, *J. Am. Chem. Soc.* **2014**, *97*, 2936; b) C. Simon, F. Rebillat, V. Herb, G. Camus, *Acta Mater.* **2017**, *124*, 579.
[30] J. L. Blackburn, A. J. Ferguson, C. Cho, J. C. Grunlan, *Adv. Mater.* **2018**, *30*, 1704386.
[31] a) C. Matthes, D. Woerner, T. Hendricks, J.-P. Fleurial, K. Oxnevad, C. Barklay, J. Zakrajsek, *"Next-generation radioisotope thermoelectric generator study"*, IEEE Aerospace Conference, Big Sky, MT, USA, **2018**, pp. 1–9, https://doi.org/10.1109/AERO.2018.8396738; b) R. M. Ambrosi, H. Williams, E. J. Watkinson, A. Barco, R. Mesalam, T. Crawford, C. Bicknell, P. Samara-Ratna, D. Vernon, N. Bannister, D. Ross, J. Sykes, M.-C. Perkinson, C. Burgess, C. Stroud, S. Gibson, A. Godfrey, R. G. Slater, M. J. Reece, K. Chen, K. Simpson, R. Tuley, M. Sarsfield, T. P. Tinsley, K. Stephenson, D. Freis, J.-F. Vigier, R. J. M. Konings, C. Fongarland, M. Libessart, et al., *Space Sci. Rev.* **2019**, *215*, 55.
[32] a) T. Zhang, X. She, Z. You, Y. Zhao, H. Fan, Y. Ding, *Appl. Energy* **2022**, *305*, 117749; b) D.-Y. Chung, T. Hogan, P. Brazis, M. Rocci-Lane, C. Kannewurf, M. Bastea, C. Uher, M. G. Kanatzidis, *Science* **2000**, *287*, 1024.
[33] J. Ahn, J.-S. Kim, Y. Jeong, S. Hwang, H. Yoo, Y. Jeong, J. Gu, M. Mahato, J. Ko, S. Jeon, J.-H. Ha, H.-S. Seo, J. Choi, M. Kang, C. Han, Y. Cho, C. H. Lee, J.-H. Jeong, I.-K. Oh, I. Park, *Adv. Energy Mater.* **2022**, *12*, 2201341.

© 2024 Wiley-VCH GmbH

15214095, 2024, 47, Downloaded from https://onlinelibrary.wiley.com/doi/10.1002/adma.202408320 by Korea University Medical Library, Wiley Online Library on [27/11/2024]. See the Terms and Conditions (https://onlinelibrary.wiley.com/terms-and-conditions) on Wiley Online Library for rules of use; OA articles are governed by the applicable Creative Commons License